Fluvial terrace formation and its impacts on early human settlement in the Hanzhong basin, Qinling Mountains, central China

Yang, Xun; Wang, Xianyan; Van Balen, Ronald T.; Prins, Maarten A.; Wang, Shejiang; van Buuren, Unze; Lu, Huayu

published in
Global and Planetary Change
2019

DOI (link to publisher)
10.1016/j.gloplacha.2019.04.007

document version
Publisher's PDF, also known as Version of record

Global and Planetary Change 178 (2019) 1–14

Contents lists available at ScienceDirect

Global and Planetary Change

journal homepage: www.elsevier.com/locate/gloplacha

Fluvial terrace formation and its impacts on early human settlement in the Hanzhong basin, Qinling Mountains, central China

Xun Yang[a], Xianyan Wang[a,*], Ronald T. Van Balen[b,c], Maarten A. Prins[b,**], Shejiang Wang[d,e], Unze van Buuren[b], Huayu Lu[a]

[a] School of Geography and Ocean Science, Nanjing University, Nanjing, China
[b] Department of Earth Sciences, Faculty of Science, Vrije Universiteit Amsterdam, Amsterdam, The Netherlands
[c] TNO – Geological Survey of the Netherlands, Utrecht, The Netherlands
[d] Key Laboratory of Vertebrate Evolution and Human Origins, Institute of Vertebrate Paleontology and Paleoanthropology, Chinese Academy of Sciences, Beijing, China
[e] CAS Center for Excellence in Life and Paleoenvironment, Beijing, China

ARTICLE INFO

Keywords:
Sedimentary environment
Floodplain
Loess
Hominin settlement
Grain size
Grain shape
Hanzhong basin

ABSTRACT

The Qinling Mountains (QLM) form the climatic boundary between the temperate north and subtropical south of China. Many important Paleolithic archaeological sites located on fluvial terraces in this area have been reported in recent decades. Abundant artifacts have been excavated in silt layers overlying fluvial gravels and coarse sands. These silt layers have thus far been interpreted as aeolian deposits. However, in principle they could also represent (in part) fluvial (floodplain) deposits, especially near the base of fine-grained sequences. Reconstruction of fluvial terrace formation is crucial for the correct interpretation of the environment of hominin occupation. In this paper, two sediment sequences from two Paleolithic sites, located on different terrace levels of the Hanjiang River in the Hanzhong basin, are studied mainly using grain-size and grain-shape analyses. In addition, grain-size distributions have been unraveled by applying end-member modelling to distinguish different sedimentary environments. The results show that three different units can be discriminated in each section. The lower unit, consisting of gravelly sand mixed with fine silt, is interpreted as shallow-channel-fill sediment deposited during the start of the transition from a channel to a floodplain environment. The middle unit comprises a fine-grained, gradually fining-upward sequence, representative a floodplain environment. At its base, it reflects a high-energy floodplain situation; at its top, the sequence is interpreted as a low-energy floodplain environment with aeolian input (settling in static water). The third, uppermost unit consists of aeolian loess interbedded with paleosol(s) and sediments that are interpreted as the results of episodic surface runoff. The gradual transition between the 3 units and the gradual fining upward trend of the middle unit indicates that there is no considerable age gap (no hiatus) between the fluvial- and aeolian sedimentary environments. Stone artifacts have been found in all 3 units, with difference abundance, indicating that both the aeolian and floodplain depositional environments provided favorable living conditions. For the floodplain environment, the resources of water and raw materials (fluvial gravels) for tool making may have offered fundamental resources for hominin settlement.

1. Introduction

The Qinling Mountains (QLM) form the climatic boundary between the temperate north and subtropical south of China (Fig. 1). In the last few decades, numerous lithic artifacts, such as handaxes and spheroids, and some rare hominin remains, such as the Yunxian man (Li and Etler, 1992), have been found and excavated in the intermontane basins of the QLM (Wang and Lu, 2016; Lu et al., 2017). These basins include the Hanzhong basin (Yan, 1980; Lu et al., 2006; Sun et al., 2012; Wang et al., 2014b; Xia et al., 2018), the Ankang basin, the Yunxian basin (Guo et al., 2013; Sun et al., 2016; Li and Li, 2017; Li et al., 2018b), and the Luonan basin (Lu et al., 2007, 2011) (Fig. 1A). In addition, stone tools have recently been reported and dated at ~2.1 Ma, at the Shangchen site in the Weihe basin in central China (see location in

* Correspondence to: X. Wang, School of Geography and Ocean Science, Nanjing University, Nanjing 210023, China.
** Correspondence to: M. A. Prins, Department of Earth Sciences, Faculty of Science, Vrije Universiteit Amsterdam, De Boelelaan 1085, 1081 HV Amsterdam, The Netherlands.
E-mail addresses: xianyanwang@nju.edu.cn (X. Wang), m.a.prins@vu.nl (M.A. Prins).

https://doi.org/10.1016/j.gloplacha.2019.04.007
Received 26 November 2018; Received in revised form 8 April 2019; Accepted 8 April 2019
Available online 11 April 2019
0921-8181/

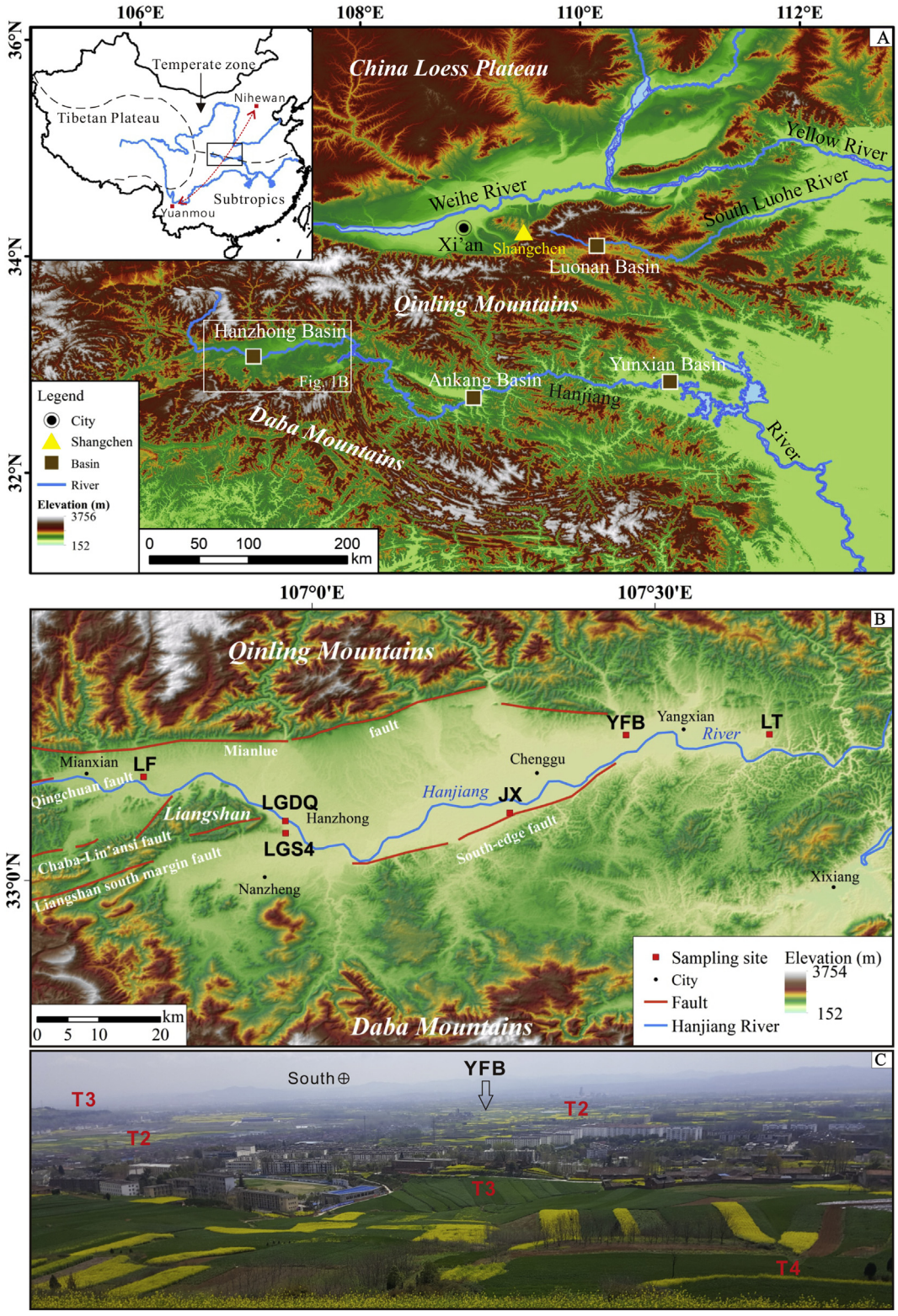

Fig. 1. (A) Digital Elevation Model (DEM) map of central China with artifact-bearing basins, including the Hanzhong basin, the Ankang basin, the Yunxian basin, and the Luonan basin. The Shangchen site (Zhu et al., 2018) is highlighted with a yellow triangle. The inset map shows the Qinling Mountains (QLM) which form the climatic boundary between the temperate north and subtropical south of China. The locations of the study area and the major hominin sites in China, including Nihewan and Yuanmou, are indicated. (B) DEM map of the Hanzhong basin bounded by the QLM in the north and the Daba Mountains in the south. The red dots indicate the locations of the two studied sites – the Fanba site in Yangxian County (YFB), the Longgangsi site on the fourth terrace (LGS4) – and the additional sites discussed in the text: the Longgang Bridge site (LGDQ), the Longting site (LT), the Liufeng site (LF), and the Jinxing site (JX). (C) Photograph of the terrace sequence in the Hanzhong basin (looking south), including YFB site. (For interpretation of the references to colour in this figure legend, the reader is referred to the web version of this article.)

Fig. 1A, ~200 km NE of the Hanzhong basin) (Zhu et al., 2018). Due to favorable paleo-environmental conditions, these intermontane basins of the QLM may have been of vital importance for the migration of hominins during the Pleistocene (Beverly et al., 2015), linking the major hominin sites in China, including the Nihewan basin in the north and the Yuanmou basin in the south (Sun et al., 2017) (Fig. 1A).

In our study area, the artifacts were excavated from fine silty, yellowish and brownish sediments. These deposits are intensively weathered, and show a massive or quite uniform structure (no bedding), as well as parting along vertical structures. For these reasons, the artifact-bearing sediments were interpreted as aeolian loess deposits in many cases (Liu, 1985; Pye, 1995; Lu et al., 2007; Sprafke and Obreht, 2016; Guo, 2017), similar to many Paleolithic archaeological sites in Europe (Einwögerer et al., 2006; Sinitsyn and Hoffecker, 2006; Boguckyj et al., 2009) and other places in China (Li and Etler, 1992; Wang et al., 2005; Lu et al., 2011; Guo et al., 2013; Li et al., 2014; Yu et al., 2017). According to Gribchenko (2006), the sites in the QLM can be considered as part of the "loessic Paleolithic" (Ranov, 1995), or the "Loessic Geoarchaeological Belt" and/or "Loess Lithic Industry" (Liu, 1999; Yang et al., 2005). This implies that hominins lived in such environments during periods of relatively cold and dry conditions (loess accumulation) as well as during relatively warm and humid intervals (paleosol formation) (Liu, 1985; Madeyska, 2002; Guo et al., 2013; Zhu et al., 2018). However, the fine-grained, loess-like sediments in the QLM accumulated on fluvial terraces, directly on top of fluvial gravel and sand (Sun et al., 2012, 2017; Li et al., 2014; Mao et al., 2017). Therefore, they could also (partly) have formed as fluvial (floodplain) deposits, especially near the base of the fine-grained sequences. A gradual transition from a fluvial (channel and floodplain) to aeolian loess accumulation on the morphological terrace surface might in principle have occurred at any particular location. Alternatively, the whole sequence of these fine-grained silty sediments might be interpreted as aeolian loess, and the abrupt environmental change, from fluvial channel (gravel and sand) to aeolian dust deposition, might indicate a sediment hiatus (age gap). An abrupt versus a gradual transition would have fundamental implications for the time-continuity of the sections and for the paleo-environmental reconstructions of the hominin presence/occupation.

In this study, we mainly use grain-size and -shape characteristics to reconstruct the paleo-environments. Grain-size distribution (GSD) is a widely used proxy to infer sediment sources and transport and deposition processes (Liu et al., 2018; Vandenberghe et al., 2018), and thus to determine paleo-environments (Omara et al., 1974; An et al., 1991; Sun et al., 2001b; Gong et al., 2005; Vandenberghe, 2013; Vandenberghe et al., 2018; Wang et al., 2015a) and paleo- climatic conditions (Lu and An, 1998; Ding et al., 2002; Sun et al., 2004; Újvári et al., 2016; Liu et al., 2018). End-member-modelling is a technique to unmix the grain size data (Weltje, 1997; Prins and Weltje, 1999; Weltje and Prins, 2003, 2007; Prins et al., 2007; Van Hateren et al., 2017). It has been used to distinguish fluvial and aeolian sedimentary components (e.g. Rits et al., 2016). Grain shape has recently been applied to the discrimination of loess transported by different wind strengths and/or under various climate conditions (Tysmans et al., 2009), to distinguish aeolian from non-aeolian contributions (Shang et al., 2017), and to differentiate alluvial and lakeshore sediments (Li et al., 2015). These studies indicate that grain shape is a powerful tool in the reconstruction of paleo-sedimentary environments, provenance, and erosion- and transport processes (Li et al., 2015).

The main objective of this work is to determine the depositional environments of the artifact-bearing sediment sequences on two fluvial terraces of the Hanjiang River in the Hanzhong basin, the main question being whether the hominins lived in a fluvial floodplain environment, on a river terrace surface on which aeolian dust was accumulating, or a combination of the two.

2. Setting and studied archaeological sites

The Hanzhong basin is located between the QLM in the north and the Daba Mountains in the south (Fig. 1B). The QLM separates cold and (semi-) arid northwestern China from warm and humid southeastern China (Fig. 1A). The QLM and the Daba Mountains are Paleozoic to Mesozoic orogenic belts. Rapid uplift of the region occurred during the Cenozoic (the late Miocene - Quaternary) due to crustal extension. Uplift has continued during the early Pleistocene to Holocene time interval (Meng and Zhang, 2000; Meng, 2017). The average altitude of the QLM is in the range of 1500–3000 m (Fig. 1A). The main peak (Mt. Taibai) has an elevation of 3767 m. The lowest elevation in the intermontane basins is ~100–200 m. The length of the QLM from west to east is approximately 800 km, and from north to south it is ~100–200 km.

The Hanzhong basin is the largest fault-related intermontane depression in the catchment of the upper Hanjiang River (Hu and Ma, 2011). The Hanjiang River, which drains this basin, is the longest tributary of the Yangtze (Fig. 1A). The Hanzhong basin has an elongated shape (W–E oriented, a similar direction as the modern Hanjiang River). A series of west–east trending faults bound the basin, e.g. the Mianlue fault in the north, the Qingchuan fault, the Chaba–Lin'ansi fault and the Liangshan south margin fault in the west, and the South-edge fault (Li et al., 2007; Zheng et al., 2016) (Fig. 1B). These faults are part of the northeastern section of the Longmenshan fault zone (Yang and Ma, 1987; Hu and Ma, 2011; Wang et al., 2013). The altitude of the Hanzhong basin is 400–800 m; its total area is ~2700 km^2 (Fig. 1B). The mean annual temperature and precipitation vary around 14–16 °C and 800–900 mm (Chen et al., 2007), respectively.

Five terraces have developed along the Hanjiang River. Their altitudes are about 3–5 (T1), 10–15 (T2), 30–40 (T3), 60–70 (T4) and 80–90 (T5) m above the present floodplain level (Yang and Ma, 1987; Wang and Lu, 2014) (Fig. 1C). They have been dated using paleomagnetic stratigraphy, luminescence dating, and soil stratigraphy of the silty, fine-grained deposits in the upper part of the terrace sequences, which overly the coarse-grained fluvial deposits (Sun et al., 2012, 2017). The age of the fifth terrace is estimated at ~1.2 Ma, the fourth at ~0.7 Ma, the third at ~0.6 Ma, and the second at 0.1–0.2 Ma (Sun et al., 2012, 2017). Abundant lithic artifacts have been found in several sedimentary layers on all terraces, except the lowest terrace (T1), which may indicate continuous early human occupation since the Middle Pleistocene (~1.2 Ma) (Wang and Lu, 2014; Wang et al., 2014b).

We studied two sedimentary sequences. The first section, at Fanba, is located in Yangxian county (YFB, 485 m altitude, N 33°12′45.8″, E 107°27′28.3″, Fig. 1B), on the second terrace (T2), on the northern bank of the Hanjiang River. An archaeological excavation was carried out in 2016 at this site (Fig. 2A); its results are still being processed. The second section, Longgangsi-T4 (LGS4, 570 m altitude, N 33°04′12.2″, E 106°57′33.9″, Fig. 1B), is located on the fourth terrace (T4), on the southern bank of the Hanjiang River. This site corresponds to Locality 3 at the Longgangsi site of Xia et al. (2018). The Longgangsi site belongs to a group of Paleolithic archaeological sites that were explored for the first time in the early 1950s (Huang and Qi, 1987), which also includes the Hejialiang (T2) and Yaochangwan (T3) sites (Sun et al., 2012; Wang et al., 2014b). The archaeological excavation at LGS4 was carried out in 2014. It covered an area of 36 m^2 (Fig. 2C) and yielded in total 4441 stone artifacts, dominated by flakes (n = 1179, 27%), chunks (n = 1636, 37%) and chips (n = 1489, 34%) (Xia et al., 2018). The majority of artifacts (n = 4406, 99%) have been collected from the upper 5 m, whereas the other pieces (n = 35, 1%) were obtained from the lowermost 8 m of the sequence (Fig. 3) (Xia et al., 2018).

3. Material and methods

One hundred and seven samples from the YFB section (Fig. 2B) and 81 samples from the LGS4 section (Fig. 2D) were taken at 10 cm

Fig. 2. (A) Paleolithic archaeological site YFB. (B) The lower part of the YFB section with sandy gravels at the bottom and trough erosion near the base. (C) Paleolithic archaeological site LGS4 with artifacts (red flags represent the location of the artifacts). (D) Sedimentological sampling of section LGS4. (For interpretation of the references to colour in this figure legend, the reader is referred to the web version of this article.)

resolution for grain-size and grain-shape analyses. The basal 5 m of LGS4 was not sampled because of collapse of the section. Twelve samples from four additional sites were also analyzed for grain size and grain shape. These additional sites were selected because they exposed clear sedimentary structures which can be linked to specific depositional (sub-) environments (e.g. channel, floodplain and aeolian). They are used for comparison with the YFB and LGS4 sediment sequences.

3.1. Grain-size analyses

GSDs (range 0.02–2000 μm with 100 size classes) were measured using a Malvern Mastersizer-2000 laser diffraction particle-size analyzer at Nanjing University. About 0.5–2 g of bulk sediment was oxidized with 10% hydrogen peroxide (H_2O_2) to remove organic components. Subsequently, to dissolve carbonates including nodules completely, 10% hydrochloric acid (HCl) was added and heated to boiling point. Next, the beaker was filled with deionized water and left standing overnight. Finally, 10 ml 0.05 mol/l sodium hexametaphosphate ($(NaPO_3)_6$) was added as a dispersing agent prior to 10 min of ultrasonic dispersion (Lu and An, 1997; Zhang et al., 2008). The GSDs were analyzed using the GRADISTAT Program (Blott and Pye, 2001). End-member modelling of all grain-size data from samples taken from the Hanzhong basin has been executed with the algorithm AnalySize-1.1.2 (Paterson and Heslop, 2015).

3.2. Grain-shape analyses

Grain shapes from 16 samples (Table S1) were analyzed by dynamic-image analysis using a Sympatec Qicpic instrument at the Vrije University Amsterdam. These samples include four floodplain samples (LGDQ-2, and JX-2, 4, 5), and one loess sample (LF-1), which are likely to represent the primary sediment environments in this study. The remaining 11 samples are from the YFB sequence (the red dots in Fig. 3B highlight the location of the samples for grain shape). The pretreatment was similar to the grain-size analyses except for the 10 min ultrasonic dispersion. The Qicpic setup applied in this study allows the analysis of several million particles within the 2–500 μm size range during 3 min measuring time (Shang et al., 2017).

The results provide information of grain shape and size. Here, the grain shape is characterized by calculating the aspect ratio values (ARs). In this case, the aspect ratio is the ratio of the minimal to maximal Feret's diameter. The aspect ratio ranges from 0 to 1, corresponding to a grain shape ranging from extremely flat or elongated to perfectly symmetrical (Li et al., 2015; Shang et al., 2017). In this study, the ARs of particles with a mean Feret's diameter between 15.6 and 62.5 μm were selected for analyses, because the shape of particles < 15.6 μm are not accurately measured by the Qicpic camera (2 μm × 2 μm pixel size; Shang et al., 2017), and because of the highly variable mean ARs in the size range > 62.5 μm, probably caused by the limited number of measured grains (Tysmans et al., 2006; Shang et al., 2017). In addition, we calculated the weighted average aspect ratio (WAAR) from 15.6 to 31.3 μm vs. WAAR from 31.3 to 62.5 μm, based on the corresponding volume frequency for the different size class. We choose 31.3 μm as the boundary because it is close to the transition between coarse silt and very coarse silt (31 μm).

4. Results

4.1. Lithostratigraphy

The basal part of the YFB section consists of a sandy gravel layer (Figs. 2B and 3A), and is covered by grey–green (2.5GY 5/2, 1040–1070 cm) and red–brown (5YR 4/4, 990–1040 cm) silty sand with abundant mica. From 830 to 990 cm, the sequence is composed of red–brown (5YR 4/4) sandy silt with an undulating pale grey (7.5GY 5/2) clay layer with erosive surface at the depth of 890 cm (Fig. 2B). This is overlain by a red–brown (5YR 4/4) silt layer at 410–830 cm with abundant black Fe−Mn films, white calcium carbonate nodules, and grey–green (2.5GY 5/2) vertical structures. In this layer a fine quartz gravel clast (about 5 mm × 3 mm × 2 mm) was found at 800 cm depth. The 300–410 cm interval consists of yellow–brown (5YR 5/6) silt with abundant black Fe−Mn nodules, white calcium carbonate nodules and a quartz granule (about 3 mm × 3 mm × 2 mm) at 320 cm in depth. The uppermost 300 cm of the sequence is composed of red–brown (5YR 4/4) silt with black Fe−Mn films and nodules, and white calcium carbonate nodules. The sizes of all the Fe−Mn nodules mentioned above are smaller than 1 mm.

The LGS4 section (Figs. 2C and 3C) is 13 m thick. The base of the

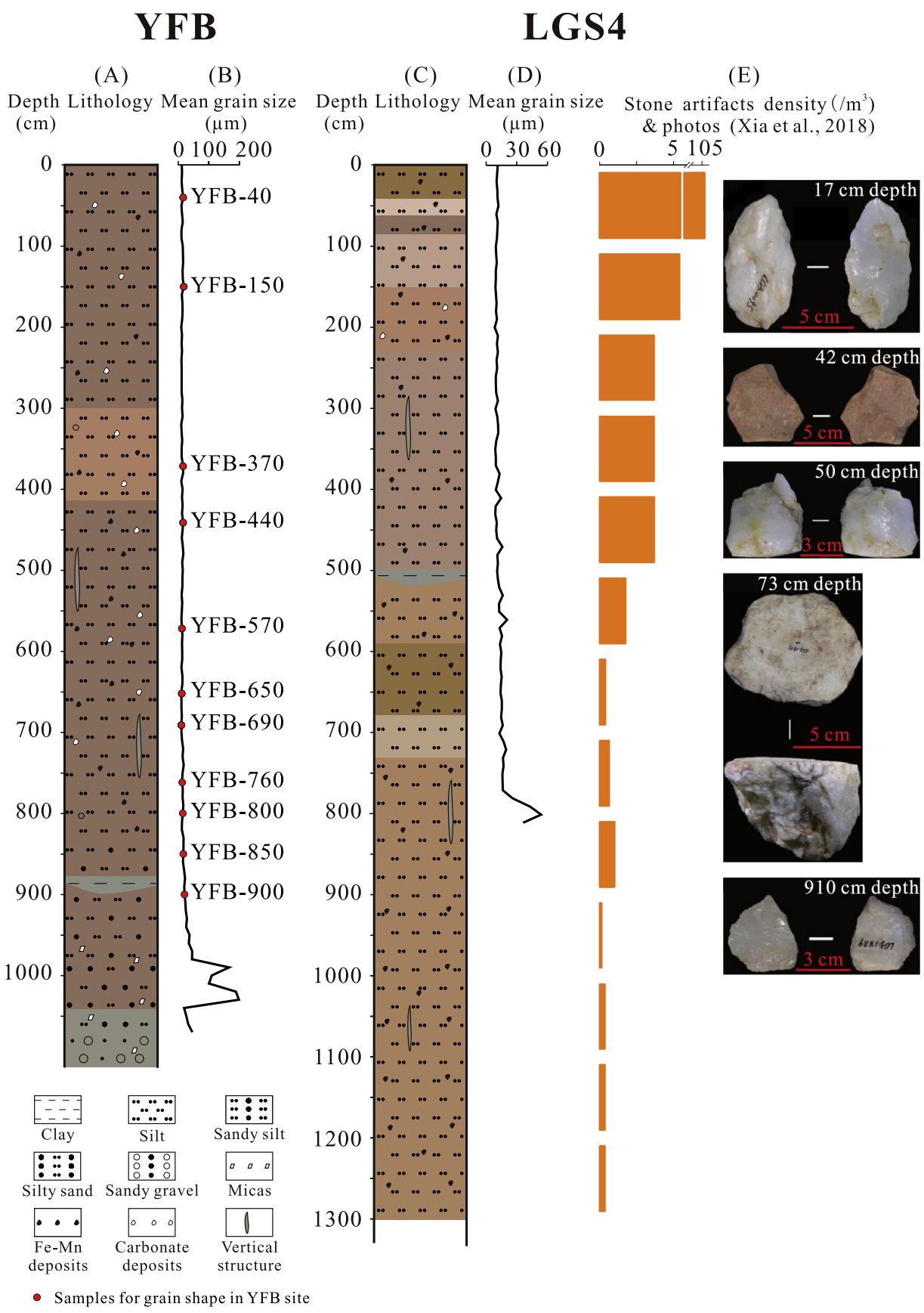

Fig. 3. (A) The lithology of the YFB section. (B) Mean grain size record of the YFB section. Red dots highlight the grain-shape samples. (C) The lithology in the LGS4 section. (D) Mean grain size record of the LGS4 section. (E) Stone artifacts density (the number of stone tools per m^3) and some photographs of the artifacts (modified from Xia et al. (2018)) in the LGS4 section. (For interpretation of the references to colour in this figure legend, the reader is referred to the web version of this article.)

terrace sequence was not exposed. In the lower part, from 1300 to 860 cm, it consists of dark brown (7.5YR 5/7) silt with abundant black Fe—Mn films, pale grey vertical structures and a loose and porous texture. At the depth of 730–860 cm, the sediments consist of dark brown (7.5YR 5.5/6) silt with black Fe—Mn nodules and pale grey vertical structures in cracks. Pale grey and yellow (10YR 6/3) silt is present from 680 to 730 cm. At the depth of 590–680 cm, the deposits are composed of brown (7.5YR 4/6) silt with abundant black Fe—Mn films, and a loose and porous texture. The overlying layer consists of brownish (7.5YR5/6) silt with abundant Fe—Mn nodules at the depth of 500–590 cm. At the depth of 230–500 cm, the sediments consist of dark brown (7.5YR 5/4) silt with Fe—Mn films and nodules, a loose and porous texture and unconformity surfaces in pale grey clay. A yellowish red (5YR 5/6) silt layer with ~5 cm sized calcium carbonate nodules is present at 150–230 cm depth. This layer is overlain by a dark orange (7.5YR 6/4) silt layer (80–150 cm) with evidence of strong pedogenesis, containing plant root cracks filled with black Fe—Mn films, and sparse black Fe—Mn nodules. The upper three layers consist of silt with black Fe—Mn films, with a loose and porous texture. They show slight differences in colour with yellowish brown silts (5YR 4/4) at 60–80 cm, reddish silts (7.5YR 7/4) at 40–60 cm and brown silts (7.5YR 4/6) at 0–40 cm.

The lithostratigraphy of the four additional sites for comparison are as follows:

Site 1, the Longgang Bridge site (LGDQ, N 33°5′13.4″, E 107°57′40.8″) in Hanzhong city, is on the first terrace (T1) of the Hanjiang River (see location in Fig. 1B). From base to top, the sediment sequence (Fig. 4A) is composed of a > 2 m thick gravel sheet with well-rounded, imbricated gravels, a ~1.6 m thick sand and silt layer with horizontal bedding, trough cross bedding and ripples (channel sample LGDQ-1), and a ~1 m thick laminated clay and silt layer (overbank sediment, sample LGDQ-2).

Site 2, the Longting section (LT, N 33°12′49.6″, E 107°40′0.8″), is located on the second terrace (T2) of the Hanjiang in the eastern part of the basin (Fig. 1B). The sediment sequence (Fig. 4B) consists of ~3 m thick loessic silty deposits (sample LT-1), which show an erosional upper boundary with an overlying paleosol, a ~3.5 m thick reddish paleosol layer (sample LT-2) and a ~5 m thick loess layer, from the base to the top.

Site 3, the Liufeng section (LF, N 33°9′5.5″, E 106°45′16.6″) is situated in the nearly westernmost tip of the Hanzhong basin, on terrace T2 of the Hanjiang (Fig. 1B). The sediment sequence is composed of a yellowish silty layer (loess) of about 0.5 m thickness (sample LF-2) between two brown silty layers (paleosols, sample LF-1) (Fig. 4C).

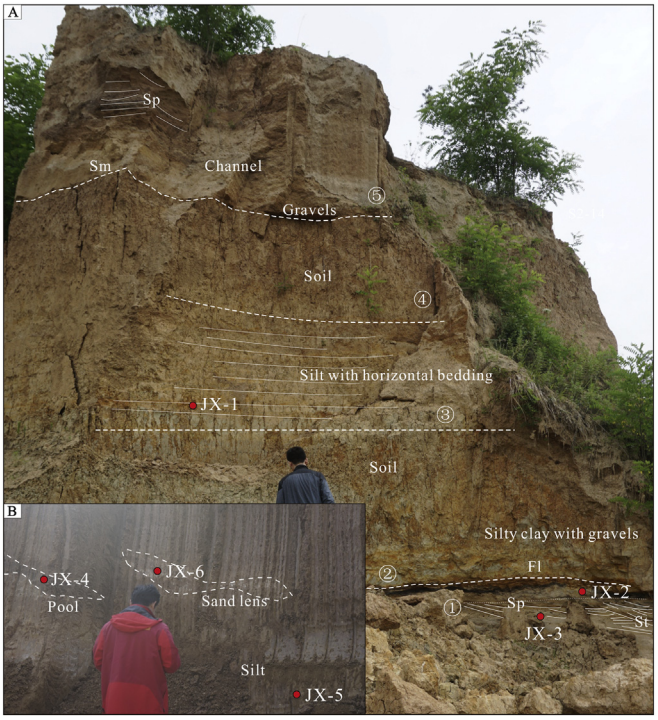

Fig. 5. (A) The JX section has a thickness of 14 m and is comprised of (from base to top): (1) Sandy gravel channel fill with trough and planar cross bedding (St/Sp). Sample JX-2 is obtained from a flood sand sheet and JX-3 from a sandy gravel channel deposit; (2) Soil and silty clay with coarse sand (floodplain); (3) Grey and brown silt layers with horizontal bedding in 10–15 cm intervals (floodplain, sample JX-1); (4) Brown paleosol with a massive structure; (5) Sandy gravel layer overlain by silts, showing channel scour (channel, Sm/Sp). (B) The uppermost part of the JX site. Sample JX-4, JX-5 and JX-6 are from a clay pool (the left dashed circle), a silt layer and a shallow secondary channel fill from floodplain environment (sand lens, the dashed circle on the right), respectively. (For interpretation of the references to colour in this figure legend, the reader is referred to the web version of this article.)

Site 4, the Jinxing site (JX, N 33°5′55.5″, E 107°17′18.2″) is located on the third terrace (T3) in the central part of the basin (Fig. 1B). The sediment sequence is approximately 14 m thick (the base is not exposed) and comprises 5 units from the top to base (Fig. 5A).

(5) A ~3 m thick sandy gravel layer with interbedded soil and silt,

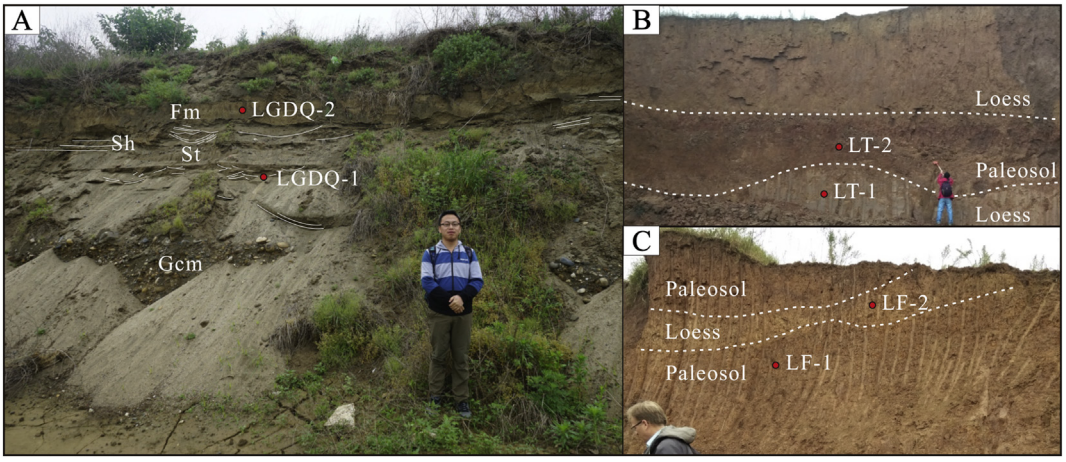

Fig. 4. (A) The LGDQ section is (from base to top) composed of well-rounded gravels with imbrication and/or sheet structure (channel deposits, Gcm), sand and silt with horizontal bedding, trough cross bedding and ripples (high energy floodplain, St and/or Sh; sample LGDQ-1), and laminated clay and silt layer (low energy floodplain, Fm; sample LGDQ-2). (B) The LT section includes (from base to top) loess deposits (sample LT-1) with distinct trough bedding, a reddish paleosol layer (LT-2) and another loess layer. (C) The LF section consists of a yellowish loess layer (sample LF-2) intercalated between two brownish paleosol layers (sample LF-1).

showing channel scour.

(4) A ~2.5 m brown soil with clay and silt grain size and a massive structure.

(3) A ~3 m thick unit composed of grey and brown silt layers with horizontal bedding at a 10–15 cm thickness interval (floodplain, sample JX-1).

(2) A ~3 m thick unit consisting of a combination of silty clay and coarse sand (low volume; floodplain).

(1) A > 2.5 m thick sandy gravel channel fill with trough and planar cross bedding; Samples JX-2 and JX-3 from this unit were obtained from flood sand sheet and sandy gravel channel deposits, respectively.

The uppermost part of the JX sequence shown in Fig. 5B includes a clay deposit (still-water sediment, sample JX-4), a silt layer (overbank sediment, sample JX-5) and a shallow secondary sand channel deposit (sand lens, sample JX-6) from a floodplain environment.

4.2. Grain size characteristics of the YFB site

Based on field observations (Fig. 3) and the GSDs (Fig. S1), three main units can be distinguished in the YFB sequence.

4.2.1. Unit 1 (1070 to 950 cm depth)

Samples in this unit are characterized by bimodal GSDs with a high proportion of sand-sized particles (Fig. 7B_8). Samples from YFB-1030 to YFB-990 (Fig. S1$_{Y26}$) are dominated by sand (on average ~68% of the volume), and are characterized by very poorly sorted and coarse-skewed GSDs. These GSDs comprise two clearly defined dominant modes: the coarser and main mode is leptokurtic with a modal size in the range 400–700 μm, whereas the finer mode illustrates a platykurtic distribution with a modal size of 30–75 μm. Samples from YFB-1070 to YFB-1040 and samples from YFB-980 to YFB-960 (Figs. S1$_{Y27}$ and S1$_{Y25}$, respectively) are characterized by an average sand content of ~38%.

4.2.2. Unit 2 (950 to 700 cm depth)

The GSDs in this unit are (very) poorly sorted and also show two modes, but the particle size is in general finer than Unit 1 (Fig. 7B). The coarser of the two modes is mesokurtic with a modal size of 200–500 μm and the finer one is mesokurtic to leptokurtic with a modal size of 13–34 μm. These samples have a mean grain size of 10–38 μm and are thus classified as medium to very coarse silt. Importantly, the percentage of sand gradually decreases upwards from ~39% to 2.5% (Fig. 7B_{5-7}) and the silt content increases upwards from 56% to 91%, while the clay fraction maintains relatively stable, varying between 5% and 11%.

4.2.3. Unit 3 (700 to 0 cm depth)

The samples from the upper unit (Fig. 7B_{1-4}) are medium to coarse silts, with an average composition of 86% silt, 8% clay and 6% sand. The GSDs are poorly sorted and again two modes can be distinguished. The coarse mode is leptokurtic with a modal size of 22–40 μm, and the fine mode is platykurtic with a modal size of 4–8 μm. The mean grain size is approximately 10–18 μm. Additionally, the GSDs of samples YFB-70, 100–150, 270–500, and 540 show a minor tail between ~200 μm and 600 μm, which accounts for < 2% (Fig. S1).

Moreover, within most of the GSDs, subordinary asymmetric modes are visible, usually at 4–8 μm and 0.6–0.9 μm.

4.3. Grain size characteristics of the LGS4 site

The overall character of the GSDs at LGS4 is similar to YFB (Fig. S2), although the mean grain size tends to be finer than at the YFB site (Fig. 3D and B, respectively).

4.3.1. Unit 1 (below 790 cm depth)

Two significant modes can be recognized in the lowest part (Fig. 7D_7). Sample LGS4-800 has a bimodal GSD, consisting of a leptokurtic and dominant mode of 300 μm, and a platykurtic and secondary mode of 21 μm. The GSD of sample LGS4-810 (Fig. S2$_{L20}$) is similar to the GSDs of samples YFB-1040 to YFB-1060. Accordingly, the depositional environment could be the same as for Unit 1 at the YFB site.

4.3.2. Unit 2 (790 to 550 cm depth)

Sample LGS4-790 (Fig. 7D_6) is composed of very coarse silt. Compared to LGS4-800, it is characterized by a higher content of the fine fraction (mode at ~40 μm) and a lower content of the coarse fraction (mode at 240 μm). This resembles sample YFB-900 in the lower part of Unit 2 at YFB (Fig. S1$_{Y23}$). Similarly, the samples with a low content of coarse fraction can be correlated with the sediments from the upper part of Unit 2 at the YFB site. Thus, the sediments in the depth interval from 550 to 790 cm are interpreted as representing a depositional environment similar to those of Unit 2 at YFB.

4.3.3. Unit 3 (550 to 0 cm depth)

Sediments from the upper 5.5 m consist of medium silt with on average 86% silt, 10% clay and 4% sand, and a mean grain size of 8–16 μm. The GSDs are poorly sorted and are unimodal with a modal size of 10–38 μm (Fig. 7D_{1-4}). Again, a very coarse tail with grain size up to 600 μm is present occasionally in Unit 3, but it contributes < 2% of the volume. Altogether these sediments resemble Unit 3 at YFB.

4.4. End-member modelling

The GSDs of all samples can be adequately described as mixtures of 5 end members (EMs) (Fig. 6A and B), as the r^2 statistics show that the five-end-member model can explain on average 99% of the total variance in the dataset. Applying more end members does not improve the result significantly. The GSDs of the 5 EMs are shown in Fig. 6C with EM1 being the coarsest and EM5 the finest. The unimodal and very coarse-skewed GSD of EM1 has a modal size of 600 μm, representing coarse sand. EM2 shows a bimodal distribution with modes at 150 μm and 13 μm. EM3 is mainly composed of coarse silt with a modal size at 38 μm. The relatively symmetrical and mesokurtic distribution of EM4 has a modal size of 15 μm, representing medium silt. Consisting dominantly of fine silt, EM5 displays a fine-skewed and mesokurtic GSD with a modal size of 6 μm.

The cumulative proportional contributions of the 5 EMs in the YFB and LGS4 sites are shown in Fig. 7A and C, respectively. Several bulk grain-size distributions are shown together with the contributing EM distributions (scaled to their proportional contribution to the bulk distribution) for illustration (Fig. 7B and D). EM1 and EM2 contribute dominantly to Unit 1, of which the contribution even reaches over 75% at the depth of 990–1030 cm at the YFB site and 800 cm at the LGS4 site. For Unit 2, the contribution of EM1 ranges from 8% to 1% and the contribution of EM2 decreases gradually upward from ~52% to 0% at the YFB site; the contribution of EM1 ranges from 3% to 0% and the contribution of EM2 decreases gradually upward from ~53% to 0% in the LGS4 section. The total volume of EM1 and EM2 exhibits a tendency to gradually decrease upward from ~56% to 0%, both at the YFB and LGS4 sites. EM1 and EM2 have relatively low percentages in Unit 2 of LGS4 compared to Unit 2 of YFB. Correspondingly, the percentage of EM4 and EM5 increases upward from 20% to average 60% in Unit 2 of YFB and from 10% to average 50% in Unit 2 of LGS4. At both sites, Unit 3 is dominated by EM4 and EM5, with average contributions of over 60% (Fig. 7B_2 and D_2). However, EM2 in Unit 3 is present in a series of spikes (coarse events), reaching levels up to 20%, especially between 350–500 and 70–150 cm at YFB. Similarly, end-member distributions of sediments of the 0–360 and 400–460 cm depth intervals of LGS4 have spikes of the coarse EM2, contributing up to 6%. As for the contributions of EM3, they fluctuate in the range 11–60% in Unit 2 and 0–60% in Unit 3.

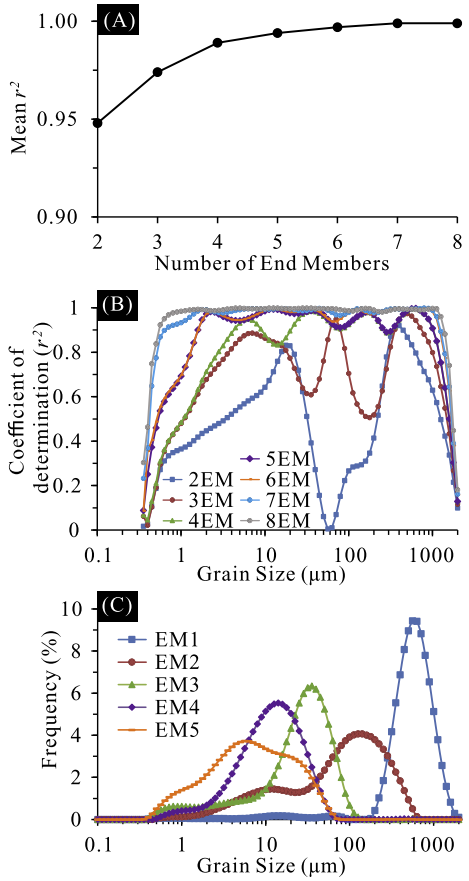

Fig. 6. End-member-modelling results. (A) Mean coefficient of determination (mean r^2) as a function of the numbers of end members. Five end members explain on average 99% of the observed variance. (B) Coefficient of determination (r^2) statistics for each size class for end member models with two to eight end-members. (C) The grain size distributions (GSDs) of the modelled end members of the five-end-member model representing coarse sand (EM1, modal size 598 μm, mean size 601 μm), very fine sand (EM2, bimodal distribution with modal size 150 μm and 13 μm, mean size 66 μm), coarse silt (EM3, modal size 38 μm, mean size 23 μm), medium silt (EM4, modal size 15 μm, mean size 12 μm), and fine silt/clayey silt (EM5, modal size 6 μm, mean size 7 μm).

4.5. Grain shape characteristics of the YFB site

In total eleven samples were chosen from the YFB sequence for grain shape analyses (Fig. 3B). For particles in the 16–63 μm size fraction in Unit 2, the ARs decrease from 0.700 to 0.538 as grain size increases (Fig. 8B and more details shown in Table S1). Sample YFB-900 from the basal part of Unit 2 displays a size-aspect ratio range which is significantly lower (0.691–0.504) than in the upper samples. Apart from sample YFB-900, the grain-shape distributions of samples from the upper part of this unit are marginally higher or equal compared with those from the lower part (Fig. 8B).

In contrast, for particles in the same size range, the ARs from Unit 3 range between 0.707 and 0.562. Again, they decrease with increasing grain size (Fig. 8A and more details shown in Table S1). The grain-shape distributions in the 16–63 μm size range are almost identical for all samples from Unit 3.

4.6. Grain-size and -shape characteristics of known depositional environments

Based on sedimentary indications for paleo-environmental interpretations (e.g. bedding), the 14 samples collected from the LT, LF, JX and LGDQ sites can be grouped into three main sedimentary environments (Fig. 9). The first group of sediment samples is of aeolian origin (Fig. 9A). The GSDs of LT-1 and LT-2 are unimodal, poorly sorted, and with a mode at 15–19 μm and a mean grain size of 11 μm. Sample LT-1 also contains a very small tail of coarse particles with size > 100 μm (0.7%), potentially related to temporary overland flow/surface runoff (see below) (Fig. 4B). This coarse component is not visible in sample LT-2. Samples LF-1 and LF-2 are also characterized by poorly-sorted GSDs with a mode at 30 μm and a shoulder at 6 μm. Sample LF-1 with a mean size 13 μm is slightly coarser than LF-2 with a mean size of 10 μm.

The second group of samples shows the variety of lithofacies characteristic for an alluvial floodplain environment (Fig. 9B). Sample LGDQ-2 is composed of fine sand with an admixture of silt and clay; its size distribution is very poorly sorted, coarse-skewed and it has a modal size of 150 μm (Fig. 9B). This sample is interpreted as reflecting a proximal, high-energy floodplain setting (e.g. proximal channel levee). Sample JX-1 is composed of fine to very coarse silt, and its well sorted GSD has a modal size of 34 μm (Fig. 9B). This sample has been collected from a clearly defined silt layer (Fig. 5A) and reflects an 'intermediate energy' floodplain setting (e.g. distal channel levee). Taken from a flood sand sheet (e.g. crevasse splay), sample JX-2 shows a very poorly sorted and strongly bimodal GSD with modes at 670 μm and 30 μm (Fig. 9B). The remaining two samples (JX-4 and 5) (Fig. 5B) consist of dominantly fine–medium silt, together with a low fraction of sand and clay, which can be considered as a typical low-energy, distal floodplain and/or fluvio-lacustrine setting. The GSD of JX-4, originating from a fluvio-lacustrine setting on a floodplain, is poorly sorted, fine-skewed and mesokurtic with a modal size of 9 μm (Fig. 9B). JX-5, from a silt layer on a floodplain, is characterized by a fine modal size (19 μm) with a coarse tail (modal size at 355 μm but lower than 1%) (Fig. 9B).

The third group of samples represents typical fluvial channel deposits. Sample LGDQ-1, JX-3 and JX-6 display poorly sorted, typical bimodal GSDs with a leptokurtic mode at ~500 μm and another broadly centered around 20–80 μm (Fig. 9C).

Selected samples for grain-shape analyses include four floodplain samples (LGDQ-2, and JX-2, 4, 5), and one loess sample (LF-1), which likely represent the potential sedimentary environments in this study (Fig. 8C and more details in Table S1). All samples show decreasing ARs with increasing grain size. However, the size–shape trend of the aeolian sample appears to differ slightly from the fluvial samples (Fig. 8C). For the aeolian sediments (sample LF-1), the ARs decreases from 0.703 to 0.565 with an increase in grain size from 16 μm to 63 μm, whereas grains from the floodplain deposits, are characterized by ARs which range from 0.663–0.507 in sample LGDQ-2, 0.694–0.528 in sample JX-2, 0.705–0.567 in sample JX-4 and 0.701–0.563 in sample JX-5, respectively (Fig. 8C).

5. Discussion

5.1. Comparison of the modelled end members with sediments from known depositional environments

EM1 can be correlated well with GSDs of samples LGDQ-1, JX-3 and the modern fluvial sands at Xifeng (Sun et al., 2001a), which are interpreted as shallow sandy channel and/or point bar deposits (Fig. 10A). The GSD of EM2 is comparable to those samples originating from high-energy active floodplains, e.g. LGDQ-2 and JX-2. The different modal sizes shown in the GSDs are possibly caused by various hydrodynamic conditions, with a higher content of coarse fraction representing higher energetic conditions. When the transporting energy becomes weaker, the volume of coarse fraction would likely reduce from JX-2 to LGDQ-2 (Fig. 10B). EM3 shows quite similar GSDs to sample JX-1, taken from a horizontal silt layer (Fig. 10C), which could have been formed by settling of aeolian silt in static water in a floodplain environment (Wang et al., 2018). EM4 is comparable to LT-1, consisting of aeolian silt (Fig. 10D). EM5, resembling LF-1, is

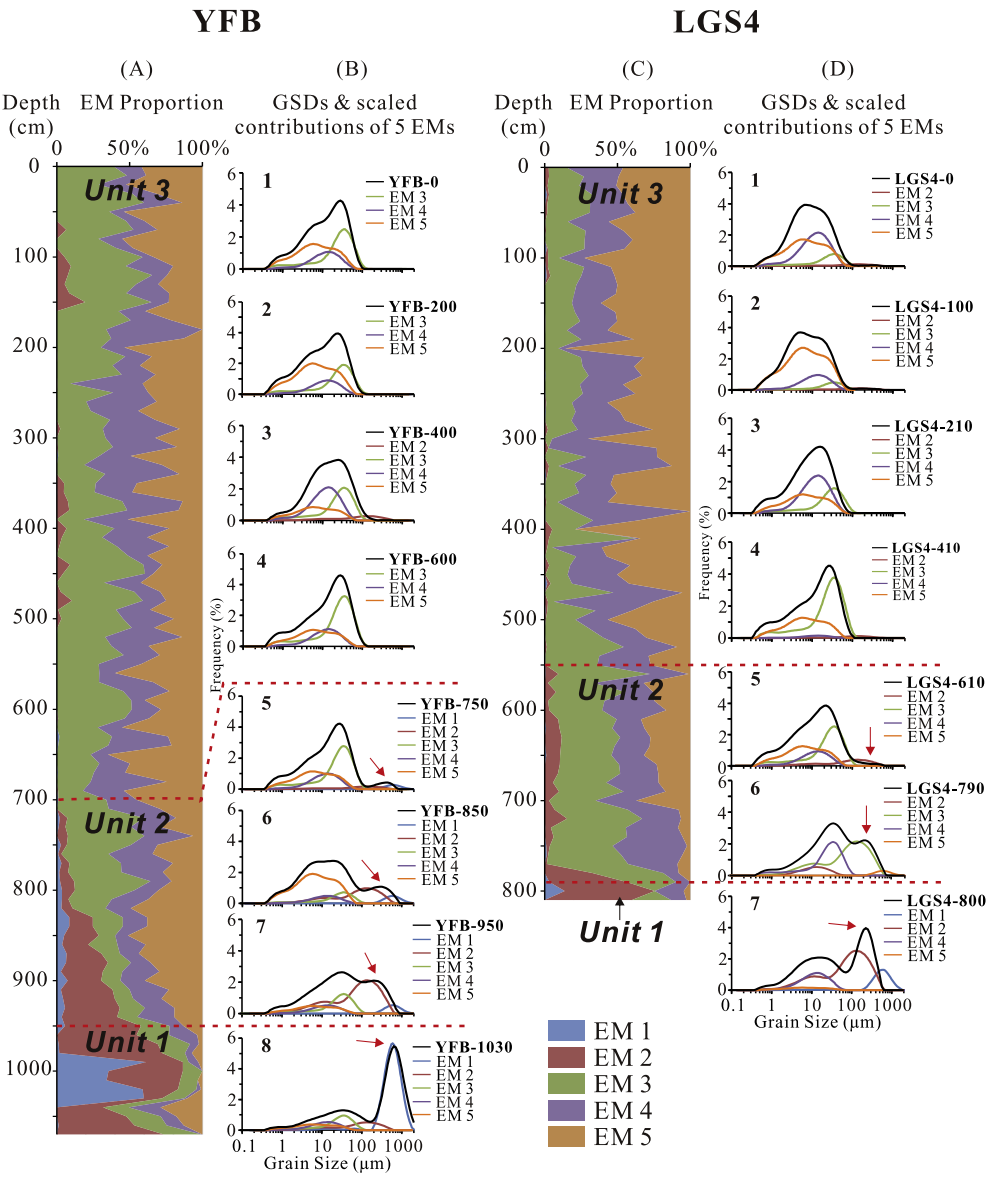

Fig. 7. Stratigraphic distribution of the end members (cumulative proportions) in sections YFB and LSG4. (A) The proportional EM contributions in section YFB. (B) GSDs of selected samples and the scaled contributions of the 5 EMs in YFB. (C) The proportional EM contributions in section LGS4. (D) GSDs of selected samples and the scaled contributions of the 5 EMs in LGS4. Note the red arrows in figures C and D highlighting the coarse mode of the grain-size distributions mentioned in the text. (For interpretation of the references to colour in this figure legend, the reader is referred to the web version of this article.)

interpreted as soil formed in loess (Fig. 10E). In addition, EM4 and EM5 can be regarded as loess sediments in the fine-silt and clay fractions (sediment type 1.c by Vandenberghe (2013)).

5.2. Depositional environment of the sediment units

Unit 1 at the base of the two sections contains abundant mica (Fig. 3A), which implies a fluvial or alluvial environment; as these platy minerals are rare in aeolian sediments they might therefore have been transported by flowing water (Rits et al., 2016). For sediments from the depth range of 990–1030 cm in the YFB section and at 800 cm depth in the LGS4 section, the GSDs show a noticeably leptokurtic mode within the medium to coarse sand range (EM1). In addition, EM2 is far more dominant in other samples of this unit (Fig. 7). Accordingly, these sediments resemble the channel or flood sand samples LGDQ-1, JX-3, and JX-6 and, in principle, they reflect a relatively high-energy environment on the floodplain, e.g. a shallow secondary channel. The silty intervals, composed of EM2 and EM3, could be interpreted as the result of settling of fine particles in standing water of abandoned pools following a peak-flow event (Vandenberghe, 2013).

Additional indications for the depositional environment of Unit 1 are provided by the results of grain-shape analyses. Fig. 11 illustrates the weight average of aspect ratio (WAAR) from 15.6 to 31.3 μm versus that from 31.3 to 62.5 μm. Sample LGDQ-2, from a high-energy floodplain, shows a low AR, i.e. a relatively flat or elongated grain shape (Figs. 8C and 11). Since the GSDs of EM2 and LGDQ-2 are comparable (Fig. 10B), it seems that LGDQ-2 might represent similar sediment sources and transportation processes as Unit 1 (or the lowest part of Unit 2) to an extent.

Altogether, we conclude that Unit 1 was formed during transition from a shallow channel to a high-energy floodplain environment, e.g. a point bar.

Unit 2 at the YFB site has a small (decimeter scale) trough at the base (Fig. 2B) and occasional millimeter-sized quartz gravel, implying low- to moderate-energy fluvial conditions. The GSDs in this unit (Figs. S1 and S2) are similar to those of samples LGDQ-2, JX-2, 4 and 5

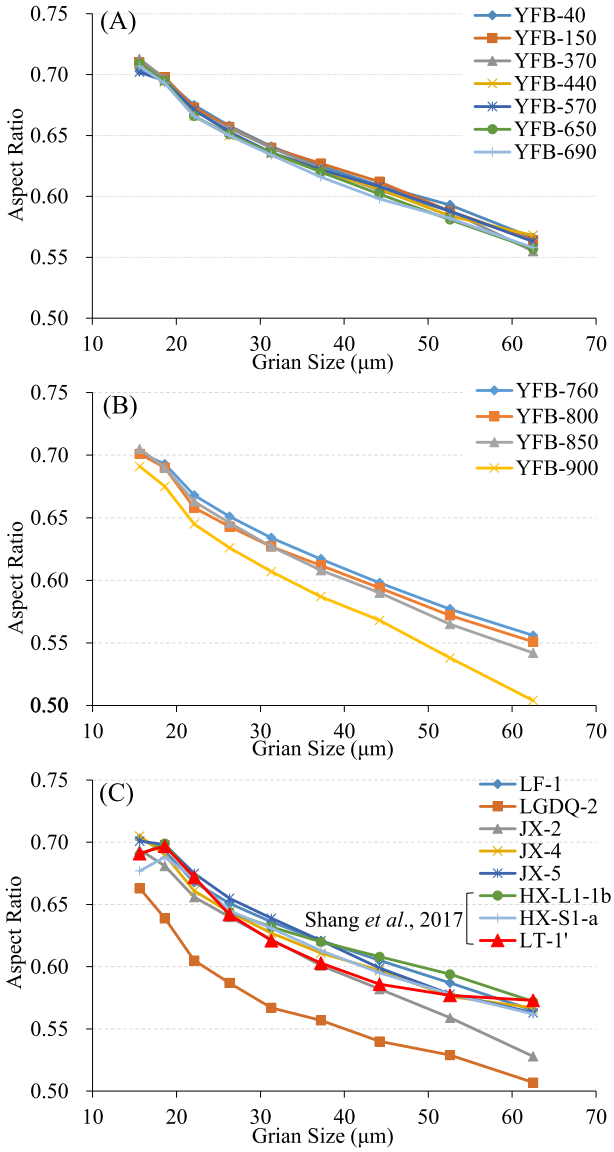

Fig. 8. Grain shape (average aspect ratio) distributions of samples from Unit 3 (A) and Unit 2 (B) of the YFB site. (C) Comparison of the grain shape (average aspect ratio) distributions of the samples from the known depositional environments to a few typical samples from the Central Loess Plateau (Shang et al., 2017).

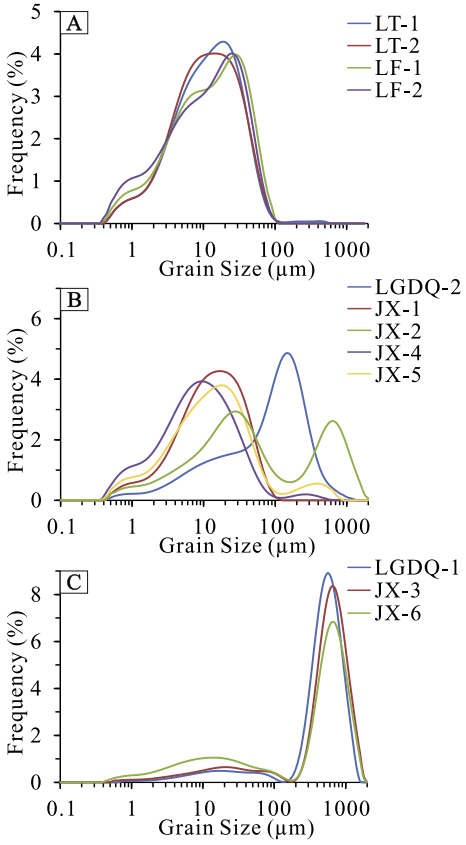

Fig. 9. (A) Grain-size distributions (GSDs) of sediments with an aeolian origin. (B) GSDs of sediments from various floodplain environments. (C) GSDs of fluvial channel deposits.

(Fig. 9B), indicating various floodplain environments.

Unit 2 at the YFB and LGS4 sites presents a clear fining-upward trend, with diminishing proportion of the sand subgroup (EM1 and EM2) and increasing contribution of silt grains (EM3, EM4 and EM5) from base to top. This could be attributed to a gradual reduction of the fluvial contribution (EM1 and EM2) and a continuous relative increase in the aeolian input (EM3, EM4 and EM5) (Fig. 7), which further represents a gradual transition from high-energy to low-energy hydrodynamic conditions.

For particles in the 26–44 μm size range, the ARs of sample JX-2 and LT-1′ (we use code LT-1′ to represent sample LT-1 in fluvial-influenced sediments (after Shang et al., 2017) to avoid confusion with our study sample LT-1) are as low as those from other samples mixed with more aeolian components (Fig. 8C). Samples YFB-900 and JX-2 display similar lower aspect-ratio distributions, suggesting they can be linked together.

Meanwhile, the WAARs of sediments in Unit 2 how an upward increase, which means their grain shapes are more and more symmetrical at depths from 900 to 760 cm in YFB (Fig. 11). Thus, they can be distinguished from the high-energy floodplain sample LGDQ-2 (Fig. 11). Deposits from Unit 2 depict similar shape features to floodplain samples (JX-2 and JX-4: obviously lower energy, compared to LGDQ-2) (Fig. 11). This implies that sediments in Unit 2 have been deposited in similar environments, where aeolian fine grains have settled in standing water or depressions on a low-energy floodplain environment. As for sample JX-5, the AR in the range of 0.701–0.563 may indicate more aeolian dust settling in a relatively low-energy floodplain environment (Fig. 8C).

Thus Unit 2 can be regarded as the transitional and gradual progression from a fluvial environment to an aeolian sedimentary environment.

Unit 3 has GSDs with typical unimodal peaks in the (very) coarse silt size class (EM-3). These GSDs resemble the type 1.b.3 aeolian loess (Vandenberghe, 2013), the aeolian sediments from Dadiwan in the western Chinese Loess Plateau (CLP) (Liu et al., 2018), and from the Yuncheng basin in the eastern CLP (Huang et al., 2007). The characteristics of sediments in Unit 3 are also quite similar to those of aeolian sediments in the study area, e.g. LT (Fig. 9A).

The mean grain sizes in the upper 2 units, Unit 2 and Unit 3, are almost identical (medium to very coarse silt size class at YFB and medium to coarse silt at LGS4, Fig. 3B and D) and the sedimentary units are too similar to distinguish in the field (Fig. 3A and C). However, with the end-member-modelling and grain-shape results, Unit 3 can be distinguished from Unit 2. Dominated by EM4 and EM5, Unit 3 contains more fine particles of probable aeolian origin than Unit 2.

Aeolian samples from the CLP (HX-L1-1b and HX-S1-a shown in Fig. 8C; after Shang et al., 2017) display aspect-ratio distributions identical with those of samples LF-1, JX-4 and JX-5, which indicates they could represent a similar sedimentary environment. Moreover, the

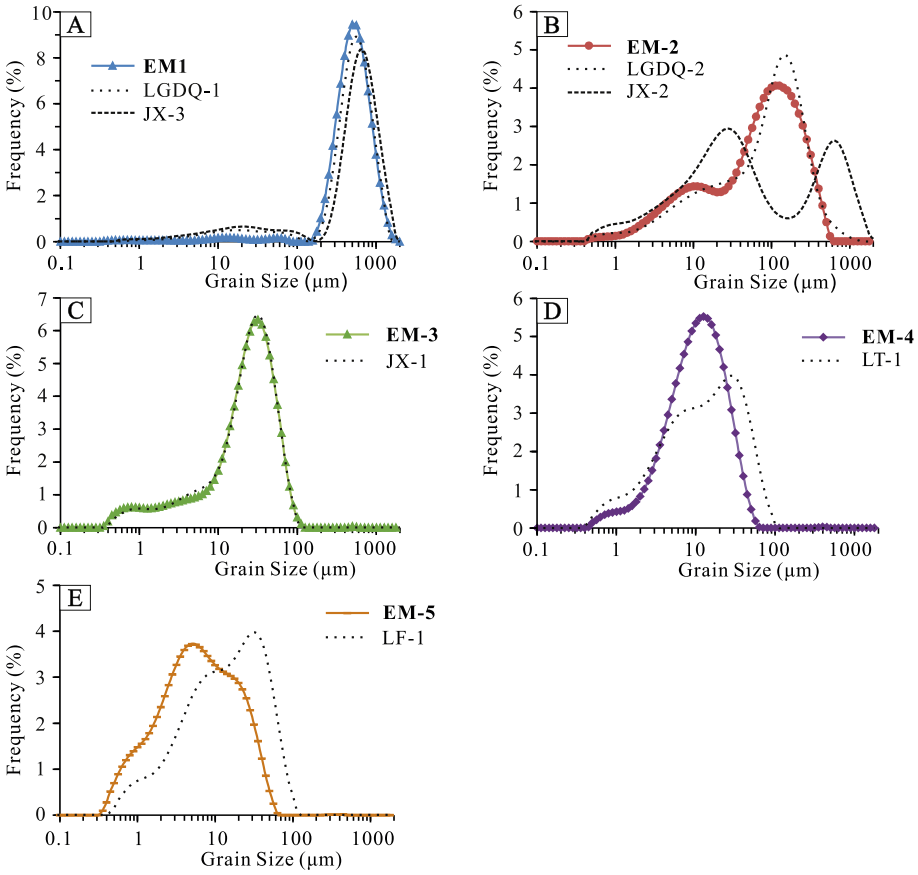

Fig. 10. Sedimentary environment interpretations of the five end members. (A) EM1compared to samples LGDQ-1 and JX-3 from shallow sandy channel and/or point bar deposits in the Hanzhong basin. (B) EM2 compared to samples LGDQ-2 and JX-2 from various high-energy fluvial settings. (C) EM3 compared with sample JX-1 which reflects relatively low-energy fluvial condition. (D) EM4 compared to sample LT-1which is interpreted as aeolian silt. (E) EM5 compared to sample LF-1 from a paleosol.

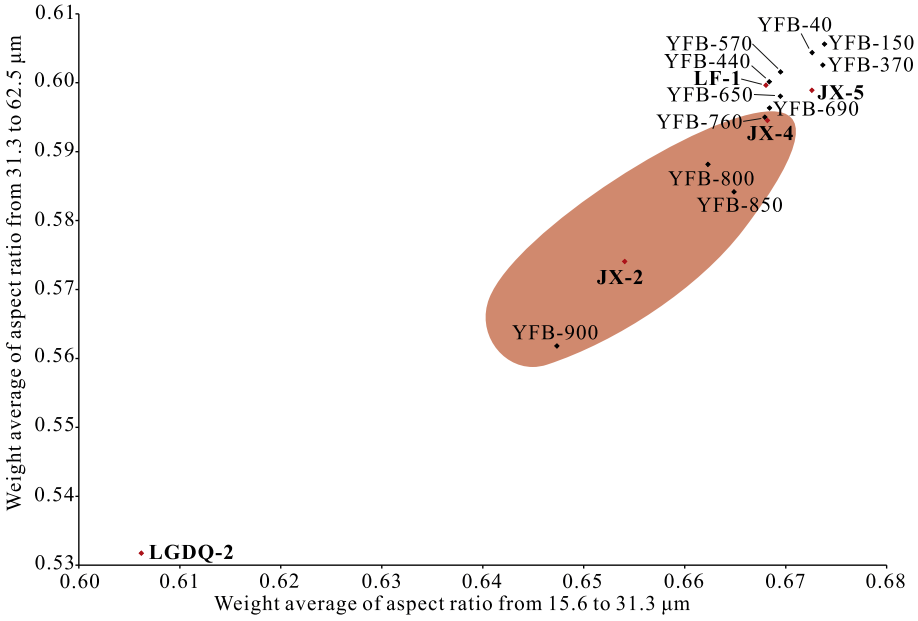

Fig. 11. Weighted average aspect ratio (WAAR) from 15.6 to 31.3 μm vs. WAAR from 31.3 to 62.5 μm. The samples plotted above the red area, including LF-1 and JX-5, represent aeolian-derived deposits, the sample plotted below (LGDQ-2) corresponds to fluvial-dominated deposits, while the samples plotted within the red area are influenced by both, aeolian and fluvial processes. (For interpretation of the references to colour in this figure legend, the reader is referred to the web version of this article.)

ARs of sediments in Unit 3 are overall higher than those in Unit 2 (Fig. 8A and B). The deposits of Unit 3 have higher WAARs both in the 15.6–3.3 and 31.3–62.5 μm size classes (Fig. 11). The data for Unit 3 show the most symmetrical grain shapes among all 3 units. Samples from Unit 3 have WAARs similar to sample LF-1. Thus, we deduce that they had similar sediment sources and/or transport and deposition processes, which is aeolian deposition with possibly some contribution from surface runoff (see discussion below). These aeolian sediments also show better sorting in grain shape (relatively concentrated ARs from different samples) as well as sorting of grain size (Fig. 11). However, the WAARs of samples from Unit 2 and Unit 3 are very similar, which implies they may in part share a similar sediment source (Fig. 8).

Noticeably, some samples from Unit 3 have a distinctive coarse fraction. For example, samples YFB-150 and LGS4-400 contain the coarse EM2 (Fig. 7A and C), which could affect the interpretation of

Table 1
The distribution and category of the stone artifacts, excavated from the sediment sequence of LGS4.

Depth(m)	Cores	Flakes	Retouched tools	Chunks	Chips	Manuports	Total
0.0–0.2	16	368	19	379	556	1	1339
0.2–0.4	17	293	9	329	307	1	956
0.4–0.6	13	291	9	463	365	7	1148
0.6–0.8	6	74	2	138	98	2	320
0.8–1.5	4	29	1	83	61	4	182
1.5–2.3	2	24	4	38	34	1	103
2.3–5.0	4	92	2	191	66	3	358
5.0–5.9	0	4	0	9	1	0	14
5.9–6.8	1	1	1	0	0	0	3
6.8–7.3	0	0	1	0	0	1	2
7.3–8.6	0	2	1	5	1	1	10
8.6–8.8	0	0	1	0	0	0	1
8.8–13.0	0	1	1	1	0	2	5
Total	63	1179	51	1636	1489	23	4441

Unit 3 to some extent. We consider that this coarse fraction could either have been transported by flowing water or it could consist of pedogenic nodules. Because of the pretreatment, carbonate nodules can be excluded, but a few Fe—Mn nodules may have survived the pretreatment process. Nevertheless, in this part of the sediment sequence, the coarse fraction cannot, in principle, be deposited by a main river channel as such a channel would probably have been incised to too great a depth for the terrace surface to have been inundated. Thus, in this case, deposits consisting of coarse components (EM2) may have been formed by temporary overland flowing water. This is in agreement with the landscape and climate setting of the study area (Wang and Lu, 2016). At present, gullies formed in aeolian deposits are ubiquitous in the piedmont areas of the Hanzhong basin (Fig. 1B). In the past, they could also have transported coarse sediments to the aeolian sequences on the terraces, as evidenced by field observations suggestive of erosion phases and sandy and pebbly interbedded deposits in the loess sequence, e.g. trough bedding at the LT site (Fig. 4B). However, such coarse fractions occur sporadically, corresponding to episodic and abrupt hydrological events in mountainous piedmont areas.

5.3. Evolution of depositional environments

The stack of different units, formed in fluvial, transitional and then dominantly aeolian sedimentary environments, implies a systematic evolution of the depositional environment at the studied sites. Fluvial dominated, channel and high-energy floodplain environments (EM1 and EM2) contribute dominantly to the lower part of the sediment sequence (Unit 1 and the lower part of Unit 2). The aeolian-dominated sediments (EM4 and EM5) progressively increase upwards. In addition, reworked (or primary) aeolian sediments (EM3) are relative stable in the middle and upper part of the sequence (Unit 2 and Unit 3) (Fig. 7).

Unit 1 consists of sediments representing channel (main channel or secondary channel) environments. It is overlain by sediments, Unit 2, deposited in a floodplain environment. This part of the sediment sequence consists of fine sand, silt and clay, up to ~2.5 m thick in both the YFB and LGS4 sections. A fining-upward cycle can arise when rivers begin down-cutting or lateral migration in response to climate change (Bridgland and Westaway, 2008; Wang et al., 2015b), base-level change (Blum and Törnqvist, 2000), and/or crustal movement (Porter et al., 1992; Vandenberghe and Maddy, 2000; Starkel, 2003; Pan et al., 2009; Cordier et al., 2017). In the above-mentioned situations, channels become inactive step by step, and will finally be abandoned. At the last stage, coarse materials (EM1 and EM2) can no longer be transported and furthermore old abandoned channels may gradually be filled by fine-grained sediment (EM3, EM4 and EM5) (Vandenberghe, 2013; Wang et al., 2018). The evolution within Unit 2, therefore, suggests a reduction of fluvial flooding activity and the enhancement of aeolian input over time. The aeolian input (e.g. EM3) may have been reworked within the floodplain environment (Huang and Qi, 1987; Vandenberghe, 2013; Liu et al., 2018; Vandenberghe et al., 2018). Nevertheless, we suggest that these two basal units represent a gradual transition from shallow channels to a high-energy floodplain and, eventually, to a low-energy floodplain environment. Sediments in this part of the sequence probably result from gradual fluvial incision in response to climatic change from cold to warm (Wang et al., 2015b, 2018). Unit 3, however, consists of aeolian deposits without reworking by fluvial floods. This can be explained by the deeper incision of the main channel of the river, causing abandonment of the floodplain during the transition from warm to cold climate (Wang et al., 2015b, 2018). Once the terrace was formed, aeolian dust could accumulate constantly (Liu, 1985), but with surface runoff.

The floodplain environment, which we identified between the fluvial-channel and aeolian deposits, is an indispensable part of the fluvial terrace formation. Furthermore, this kind of transition of sedimentary environment might indicate that there is not an abrupt but a continuous and gradual change in sedimentary environment, at least between the upper 2 units. No considerable age gap is indicated between the fluvial- and aeolian-dominated sediments. This would imply that the age of the base of Unit 3 is equivalent to the time of terrace abandonment.

5.4. Potential influence of the evolving depositional environment on human settlement

The artifacts excavated from LGS4 were made of local raw materials in cobbles/pebble form, derived from Hanjiang River gravels, among which quartz and igneous rocks are dominant (Xia et al., 2018). Artifact size and lithology were thus dictated by differences in transported gravel sizes and types (e.g. Van den Biggelaar et al., 2017). In addition, the small-sized stone-tool assemblage excavated from LGS4 (Table 1; Xia et al., 2018) is markedly different from the common Acheulean tool types in and around the QLM, which are characterized by large-sized retouched tools, such as handaxes and choppers (Huang and Qi, 1987). However, interpretations of this observation require further study.

Artifacts were present in all 3 units, not just in Unit 3, which represents aeolian loess deposit on the terrace (Fig. 3E; modified from Xia et al. (2018)). This indicates that the occupation of hominins in the QLM was continuous, and that the floodplain was also suitable for early human occupation. This can be explained by the convenience of fishing, access to water, and gravel for tool-making along the river (Wang and Lu, 2016). Similar hominin environments have been proposed for sites in Africa, Europe, and Asia (Chauhan et al., 2017; Li et al., 2018a). There is no doubt that a settlement close to a river will be in danger of flooding (Huang et al., 2013; Wang et al., 2014a; Guo et al., 2015; Liu et al., 2015; Wu et al., 2016), but the choice for a settlement location may involve other factors including water supply, food source (vegetation and animals), transport route and defense (Vandenberghe, 2015;

Schulte and Lehmkuhl, 2017).

Only 35 artifacts were unearthed from the floodplain environment, in the lower 8 m of LGS4 site. The artifact density seems relatively low (< 1 artifact/m^3) compared to the upper part, the aeolian sediments (Unit 3) (Fig. 3E). This might imply that the number of hominins on the floodplain environment was much less compared to the aeolian sedimentary environment on the terrace. This may indicate climate impacts on human occupation, but it might also be related to the morphological, elevated terrace position during the aeolian phase, with less risk of flooding. On the other hand, the high density of artifacts in the aeolian sedimentary environment (Unit 3) is more likely a result of the low sedimentation rate of aeolian sediments, allowing for more artifacts to be manufactured and to be buried into the sedimentary sequence, compared with rapid accumulation floodplain environment (Unit 2).

6. Conclusions

The Hanzhong- and other basins in the QLM have been occupied by hominins continuously since the Middle Pleistocene. A large number of stone artifacts were collected from Paleolithic sites on fluvial terraces of the upper Hanjiang River. Based on sedimentary structures, sediment grain size (especially grain-size distributions and end-member-modelling), grain shape (aspect-ratio measurements by dynamic-image analysis), and by comparison to characteristic samples from certain sedimentary environments, 3 main units/sedimentary environments can be distinguished in the studied sites.

The basal unit consists of relatively coarse-grained sediments, composed of sand and fine gravel. It is overlain by a fining-upward sediment sequence, characterized by a diminishing contribution of fluvial deposits and relatively increasing aeolian input upward. Thus, sediments in these two parts show a gradual transitional environment from fluvial channels to a high-energy floodplain, continuing to a lowering-energy floodplain. This may represent fluvial incision resulting from a change of cold to warm climatic conditions. The uppermost unit consists of aeolian sediments, likely deposited during relatively cold and dry periods. The aeolian sediments are interbedded with paleosols, formed during relatively warmer and/or more humid climate conditions, and coarse-grained particles with low volume are formed by episodic surface runoff.

Furthermore, this transitional sedimentary evolution indicates that there is no considerable age gap between the fluvial and aeolian-dominated sediments. In situ stone artifacts have been found in all 3 units, which indicates that not only an aeolian sedimentary environment on river-terrace surfaces, but also a floodplain environment was occupied by hominins, probably because of the availability of fresh water and raw materials for making tools. Furthermore, it implies that hominins lived continuously in the Hanzhong basin, and might not be dependent of the paleo-environmental and/or climatic conditions.

Supplementary data to this article can be found online at https://doi.org/10.1016/j.gloplacha.2019.04.007.

Acknowledgements

This research is supported by the National Natural Science Foundation of China (41522101, 41472026), National key research and development program (2016YFA0600500), Royal Netherlands Academy of Arts and Sciences (Chinese Exchange Program, grant number 530-5CDP07), the CAS Strategic Priority Research Program Grant B “Macroevolutionary Processes and Paleoenvironments of Major Historical Biota” (No. XDPB05), and the Fundamental Research Funds for the Central Universities (020914380043). The authors thank two anonymous reviewers and the editor, David R. Bridgland, for their constructive suggestions and linguistic improvement. We are very grateful to Jef Vandenberghe for encouraging this work and Wenting Xia for discussion. We thank Shuangwen Yi, Bin Yang, Junfei Ma, Yan Dai, Yang Yu, Quanxu Hu, Linman Gao, Zhengchen Li, Bingling Wang, Xinghua Xu, Yu Lu and Kexin Wang for their help.

References

An, Z.S., Kukla, G., Porter, S.C., Xiao, J.L., 1991. Late quaternary dust flow on the chinese Loess Plateau. Catena 18 (2), 125–132.
Beverly, E.J., et al., 2015. Recurrent spring-fed rivers in a Middle to late Pleistocene semi-arid grassland: implications for environments of early humans in the Lake Victoria Basin, Kenya. Sedimentology 62 (6), 1611–1635.
Blott, S.J., Pye, K., 2001. Gradistat: a grain size distribution and statistics package for the analysis of unconsolidated sediments. Earth Surf. Process. Landf. 26 (11), 1237–1248.
Blum, M.D., Törnqvist, T.E., 2000. Fluvial responses to climate and sea-level change: a review and look forward. Sedimentology 47 (s1), 2–48.
Boguckyj, A.B., Lanczont, M., Lacka, B., Madeyska, T., Sytnyk, O., 2009. Age and the palaeoenvironment of the West Ukrainian palaeolithic: the case of Velykyi Glybochok multi-cultural site. J. Archaeol. Sci. 36 (7), 1376–1389.
Bridgland, D., Westaway, R., 2008. Climatically controlled river terrace staircases: a worldwide Quaternary phenomenon. Geomorphology 98 (3), 285–315.
Chauhan, P.R., et al., 2017. Fluvial deposits as an archive of early human activity: progress during the 20 years of the Fluvial Archives Group. Quat. Sci. Rev. 166, 114–149.
Chen, H., Guo, S.L., Xu, C.Y., Singh, V.P., 2007. Historical temporal trends of hydro-climatic variables and runoff response to climate variability and their relevance in water resource management in the Hanjiang basin. J. Hydrol. 344 (3), 171–184.
Cordier, S., et al., 2017. The Fluvial Archives Group: 20 years of research connecting fluvial geomorphology and palaeoenvironments. Quat. Sci. Rev. 166, 1–9.
Ding, Z.L., et al., 2002. Stacked 2.6-Ma grain size record from the Chinese loess based on five sections and correlation with the deep-sea $\delta^{18}O$ record. Paleoceanography 17 (3), 1–21.
Einwögerer, T., et al., 2006. Upper Palaeolithic infant burials. Nature 444 (7117), 285.
Gong, H.J., Zhang, Y.X., Huang, L., 2005. Paleoenvironment significance of grain-size composition of Neogene Red Clay in Linxia Basin, Gansu province (in Chinese with English abstract). Acta Sedimentol. Sin. 23 (2), 260–267.
Gribchenko, Y.N., 2006. Lithology and stratigraphy of loess-soil series and cultural layers of late Paleolithic campsites in Eastern Europe. Quat. Int. 152 (3), 153–163.
Guo, Z.T., 2017. Loess Plateau attests to the onsets of monsoon and deserts (in Chinese). Sci. Sin. Terrae 47 (4), 421–437.
Guo, Y.Q., et al., 2013. Sedimentological study of the stratigraphy at the site of Homo erectus yunxianensis in the upper Hanjiang River valley, China. Quat. Int. 300, 75–82.
Guo, Y.Q., et al., 2015. Investigating extreme flood response to Holocene palaeoclimate in the Chinese monsoonal zone: a palaeoflood case study from the Hanjiang River. Geomorphology 238, 187–197.
Hu, G.R., Ma, B.Q., 2011. A preliminary Quaternary geological and geomorphic study of Hanzhong Basin (in Chinese with English abstract). Bull. Inst. Crustal Dyn. 23, 77–85.
Huang, W.W., Qi, G.Q., 1987. Preliminary observation of Liangshan Paleolithic site (in Chinese with English abstract). Acta Anthropol. Sin. 6 (3), 236–244.
Huang, C.C., et al., 2007. Impact of monsoonal climatic change on Holocene overbank flooding along Sushui River, middle reach of the Yellow River, China. Quat. Sci. Rev. 26 (17), 2247–2264.
Huang, C.C., et al., 2013. Extraordinary hydro-climatic events during the period AD 200–300 recorded by slackwater deposits in the upper Hanjiang River valley, China. Palaeogeogr. Palaeoclimatol. Palaeoecol. 374 (433), 274–283.
Li, T.Y., Etler, D.A., 1992. New Middle Pleistocene hominid crania from Yunxian in China. Nature 357 (6377), 404.
Li, C.R., Li, H., 2017. L'étude des bifaces de la Hanshui River Valley, Chine (in French with English abstract). L'Anthropologie 121 (3), 243–254.
Li, S.Z., et al., 2007. Collision leading to multiple-stage large-scale extrusion in the Qinling orogen: insights from the Mianlue suture. Gondwana Res. 12 (1), 121–143.
Li, H., et al., 2014. The Middle Pleistocene handaxe site of Shuangshu in the Danjiangkou Reservoir Region, Central China. J. Archaeol. Sci. 52, 391–409.
Li, D.W., Kang, Y.R., Li, D.W., 2015. Comparison of grain-size and grain-shape characters of alluvial and lakeshore sands based on dynamic image analysis (in Chinese with English abstract). Quat. Sci. 35 (2), 484–492.
Li, H., Li, Z.Y., Lotter, M.G., Kuman, K., 2018a. Formation processes at the early late Pleistocene archaic human site of Lingjing, China. J. Archaeol. Sci. 96, 73–84.
Li, Y.H., Zhou, Y.D., Sun, X.F., Li, H., 2018b. New evidence of a lithic assemblage containing in situ late Pleistocene bifaces from the Houfang site in the Hanshui River Valley, Central China. C. R. Palevol 17 (1), 131–142.
Liu, T.S., 1985. Loess and the Environment (in Chinese). Science press, Beijing, pp. 1–481.
Liu, T.S., 1999. Loess stone artifact industry. In: Xu Qinqi Ed. New Developments of Prehistoric Archaeology. Science Press, Beijing, pp. 52–62 (in Chinese).
Liu, T., et al., 2015. Late Pleistocene and Holocene palaeoflood events recorded by slackwater deposits in the upper Hanjiang River valley, China. J. Hydrol. 529 (10), 499–510.
Liu, X.X., Sun, Y.B., Vandenberghe, J., Li, Y., An, Z.S., 2018. Palaeoenvironmental implication of grain-size compositions of terrace deposits on the western Chinese Loess Plateau. Aeolian Res. 32, 202–209.
Lu, H.Y., An, Z.S., 1997. The influence of pre-treatment on grain-size analysis results of loess (in Chinese with English abstract). Chin. Sci. Bull. 42 (23), 2535–2538.
Lu, H.Y., An, Z.S., 1998. Paleoclimatic significance of grain size of loess-palaeosol deposit in Chinese Loess Plateau. Sci. China D 41 (6), 626–631.
Lu, N., Huang, W.W., Yin, S.P., Hou, Y.M., 2006. A new study on the Paleolithic materials from Liangshan site (in Chinese with English abstract). Acta Anthropol. Sin. 25 (2), 143–152.

Lu, H.Y., et al., 2007. A preliminary survey on loess deposit in eastern Qinling Mountains (Central China) and its implication for estimating age of the Pleistocene lithic artifacts (in Chinese with English abstract). Quat. Sci. 27 (4), 559–567.
Lu, H.Y., et al., 2011. Multiphase timing of hominin occupations and the paleoenvironment in Luonan Basin, Central China. Quat. Res. 76 (1), 142–147.
Lu, H.Y., et al., 2017. Earth surface processes and their effects on human behavior in monsoonal China during the Pleistocene-Holocene epochs. J. Geogr. Sci. 27 (11), 1311–1324.
Madeyska, T., 2002. Evidence of climatic variations in loess and cave Palaeolithic sites of southern Poland and western Ukraine. Quat. Int. 91 (1), 65–73.
Mao, P.N., et al., 2017. Loess deposits of the upper Hanjiang River valley, south of Qinling Mountains, China: implication for the pedogenic dynamics controlled by paleomonsoon climate evolution. Aeolian Res. 25, 63–77.
Meng, Q.R., 2017. Origin of the Qinling mountains (in Chinese). Sci. Sin. Terrae 47 (4), 412–420.
Meng, Q.R., Zhang, G.W., 2000. Geologic framework and tectonic evolution of the Qinling orogen, Central China. Tectonophysics 323 (3), 183–196.
Omara, S., Bishara, W.W., Nasr, M., 1974. Grain-size parameters and paleoenvironments of the Nubia Sandstone. J. Sediment. Res. (1), 136–144.
Pan, B.T., et al., 2009. Evaluating the role of climate and tectonics during non-steady incision of the Yellow River: evidence from a 1.24Ma terrace record near Lanzhou, China. Quat. Sci. Rev. 28 (27), 3281–3290.
Paterson, G.A., Heslop, D., 2015. New methods for unmixing sediment grain size data. Geochem. Geophys. Geosyst. 16 (12), 4494–4506.
Porter, S.C., Zhisheng, A., Hongbo, Z., 1992. Cyclic Quaternary alluviation and terracing in a nonglaciated drainage basin on the north flank of the Qinling Shan, Central China. Quat. Res. 38 (2), 157–169.
Prins, M.A., Weltje, G.J., 1999. End-member modelling of siliciclastic grain-size distributions: the late Quaternary record of eolian and fluvial sediment supply to the Arabian Sea and its paleoclimate significance. In: Harbaugh, J. (Ed.), Numerical Experiments in Stratigraphy: Recent Advances in Stratigraphic and Sedimentologic Computer Simulations. SEPM (Society for Sedimentary Geology) Special Publication, pp. 91–111.
Prins, M.A., et al., 2007. Late Quaternary aeolian dust input variability on the Chinese Loess Plateau: inferences from unmixing of loess grain-size records. Quat. Sci. Rev. 26 (1), 230–242.
Pye, K., 1995. The nature, origin and accumulation of loess. Quat. Sci. Rev. 14 (7), 653–667.
Ranov, V., 1995. The 'loessic palaeolithic' in South Tadjikistan, Central Asia: its industries, chronology and correlation. Quat. Sci. Rev. 14 (7), 731–745.
Rits, D.S., et al., 2016. Facies analysis of the Middle and late Quaternary sediment infill of the northern Weihe Basin, Central China. J. Quat. Sci. 31 (2), 152–165.
Schulte, P., Lehmkuhl, F., 2017. The difference of two laser diffraction patterns as an indicator for post-depositional grain size reduction in loess-paleosol sequences. Palaeogeogr. Palaeoclimatol. Palaeoecol. 1–11.
Shang, Y., Kaakinen, A., Beets, C.J., Prins, M.A., 2017. Aeolian silt transport processes as fingerprinted by dynamic image analysis of the grain size and shape characteristics of Chinese loess and Red Clay deposits. Sediment. Geol. 1–13.
Sinitsyn, A.A., Hoffecker, J.F., 2006. Radiocarbon dating and chronology of the early Upper Paleolithic at Kostenki. Quat. Int. 152 (3), 164–174.
Sprafke, T., Obreht, I., 2016. Loess: rock, sediment or soil-what is missing for its definition? Quat. Int. 399, 198–207.
Starkel, L., 2003. Climatically controlled terraces in uplifting mountain areas. Quat. Sci. Rev. 22 (20), 2189–2198.
Sun, D.H., et al., 2001a. A mathematical method for separating grain size components in sediments and its application in Paleoenvironment (in Chinese). Prog. Nat. Sci. 11, 269–276.
Sun, Q.L., Zhou, J., Xiao, J.L., 2001b. Grain-size characteristics of Lake Daihai sediments and its paleoenvironment significance (in Chinese with English abstract). Mar. Geol. Quat. Geol. 21 (1), 93–95.
Sun, D.H., et al., 2004. Bimodal grain-size distribution of Chinese loess, and its palaeoclimatic implications. Catena 55 (3), 325–340.
Sun, X.F., Lu, H.Y., Wang, S.J., Yi, S.W., 2012. Ages of Liangshan Paleolithic sites in Hanzhong Basin, Central China. Quat. Geochronol. 10, 380–386.
Sun, X.F., et al., 2016. Pedostratigraphy of aeolian deposition near the Yunxian Man site on the Hanjiang River terraces, Yunxian Basin, Central China. Quat. Int. 400, 187–194.
Sun, X.F., et al., 2017. Early human settlements in the southern Qinling Mountains, Central China. Quat. Sci. Rev. 164, 168–186.
Tysmans, D., et al., 2006. Size and shape analysis of sedimentary grains by automated dynamic image analysis. Part. Part. Syst. Charact. 23 (5), 381–387.
Tysmans, D., et al., 2009. Heterogeneity in homogeneous Brabantian loess during the late Pleniglacial. Quat. Int. 198 (1), 195–203.
Újvári, G., Kok, J.F., Varga, G., Kovács, J., 2016. The physics of wind-blown loess: implications for grain size proxy interpretations in Quaternary paleoclimate studies. Earth Sci. Rev. 154, 247–278.
Van den Biggelaar, D., Van Balen, R., Kluiving, S., Verpoorte, A., Alink, M., 2017. Gravel size matters: Early Middle Palaeolithic artefacts made from local Rhine and Meuse deposits in the central Netherlands. Neth. J. Geosci. 96, 261–271.
Van Hateren, J.A., Prins, M.A., Van Balen, R.T., 2017. On the genetically meaningful decomposition of grain-size distributions: a comparison of different end-member modelling algorithms. Sediment. Geol. 1–23.
Vandenberghe, J., 2013. Grain size of fine-grained windblown sediment: a powerful proxy for process identification. Earth Sci. Rev. 121, 18–30.
Vandenberghe, J., 2015. River terraces as a response to climatic forcing: formation processes, sedimentary characteristics and sites for human occupation. Quat. Int. 370, 3–11.
Vandenberghe, J., Maddy, D., 2000. The significance of fluvial archives in geomorphology. Geomorphology 33 (3), 127–130.
Vandenberghe, J., Sun, Y.B., Wang, X.Y., Abels, H.A., Liu, X.X., 2018. Grain-size characterization of reworked fine-grained aeolian deposits. Earth Sci. Rev. 177, 43–52.
Wang, S.J., Lu, H.Y., 2014. Current perspectives on Paleolithic archaeology in the Upper Hanjiang River Valley, Central China (in Chinese with English abstract). Acta Anthropol. Sin. 33 (3), 315–328.
Wang, S.J., Lu, H.Y., 2016. Taphonomic and paleoenvironmental issues of the Pleistocene loessic Paleolithic sites in the Qinling Mountains, Central China (in Chinese with English abstract). Sci. China Earth Sci. 59 (8), 1519–1528.
Wang, S.J., et al., 2005. Lithic artefacts collected from open-air sites during 1995—1999 investigations in Luonan Basin, China (in Chinese with English abstract). Acta Anthropol. Sin. 24 (2), 87–103.
Wang, M.M., Zhou, B.G., Yang, X.P., Xie, C., Gao, X.L., 2013. Characteristics of late-Quaternary activity and seismic risk of the northeastern section of the Longmenshan fault zone. Acta Geol. Sin. 87 (6), 1674–1689 (English Edition).
Wang, L.S., Huang, C.C., Pang, J.L., Zha, X.C., Zhou, Y.L., 2014a. Paleofloods recorded by slackwater deposits in the upper reaches of the Hanjiang River valley, middle Yangtze River basin, China. J. Hydrol. 519, 1249–1256.
Wang, S.J., et al., 2014b. Newly discovered Paleolithic open-air sites in Hanzhong Basin in upper valley of Hanjiang River and their ages (in Chinese with English abstract). Acta Anthropol. Sin. 33 (2), 125–136.
Wang, J.Z., Li, A.C., Xu, K.H., Zheng, X.F., Huang, J., 2015a. Clay mineral and grain size studies of sediment provenances and paleoenvironment evolution in the middle Okinawa Trough since 17 ka. Mar. Geol. 366, 49–61.
Wang, X.Y., Vandenberghe, J., Yi, S.W., Balen, R.V., Lu, H.Y., 2015b. Climate-dependent fluvial architecture and processes on a suborbital timescale in areas of rapid tectonic uplift: an example from the NE Tibetan Plateau. Glob. Planet. Chang. 133, 318–329.
Wang, X.Y., et al., 2018. Interaction of fluvial and eolian sedimentation processes, and response to climate change since the last glacial in a semiarid environment along the Yellow River. Quat. Res. 1–14.
Weltje, G.J., 1997. End-member modeling of compositional data: numerical-statistical algorithms for solving the explicit mixing problem. Math. Geosci. 29, 503–549.
Weltje, G.J., Prins, M.A., 2003. Muddled or mixed? Inferring palaeoclimate from size distributions of deep-sea clastics. Sediment. Geol. 162 (1), 39–62.
Weltje, G.J., Prins, M.A., 2007. Genetically meaningful decomposition of grain-size distributions. Sediment. Geol. 202 (3), 409–424.
Wu, Q.L., et al., 2016. Outburst flood at 1920 BCE supports historicity of China's Great Flood and the Xia dynasty. Science 353 (6299), 579–582.
Xia, W.T., et al., 2018. Lithic artifacts excavated from Locality 3 of the Longgangsi site in Hanzhong Basin, Shaanxi province (in Chinese with English abstract). Acta Anthropol. Sin. 37 (4), 529–541.
Yan, J.Q., 1980. Industry first discovery of the implements of the Old Stone Age at Longgang, Hanzhong, Shanxi (in Chinese). Archaeol. Cult. Relics 4, 1–5.
Yang, X.F., Ma, S.L., 1987. Geomorphological characteristics relating to the Neotectonics in the Hanzhong Basin (in Chinese with English abstract). J. Northwest Normal Univ. 2, 45–49.
Yang, X.Y., Xia, Z.K., Liu, T.S., 2005. Loess research and Paleolithic archaeology in China (in Chinese with English abstract). Quat. Sci. 25 (4), 461–466.
Yu, Q.Y., et al., 2017. A preliminary report on the 2013 excavation of the Huaishuping Paleolithic site in Luonan Basin, Shaanxi Province (in Chinese with English abstract). Acta Anthropol. Sin. 36 (2), 154–164.
Zhang, H.Y., Lu, H.Y., Zhao, J., Zhao, C.F., Zhang, P., 2008. Effects of ultrasonic dispersion on granulometry of fine-grain loess (in Chinese with English abstract). Acta Sedimentol. Sin. 26 (3), 494–500.
Zheng, W.J., et al., 2016. Geometry and late Pleistocene slip rates of the Liangdang-Jiangluo fault in the western Qinling mountains, NW China. Tectonophysics 687, 1–13.
Zhu, Z.Y., et al., 2018. Hominin occupation of the Chinese Loess Plateau since about 2.1 million years ago. Nature 559, 608–612.